Experimental Investigation on Bead Growth and Dispersion under Low-Speed Icing Condition

Yu-Eop Kang[1], Seungin Min[1], Taeseong Kim[2], Kwanjung Yee[1]

[1] *Department of Aerospace Engineering, Seoul National University, Korea*
[2]*Department of Wind Energy, Technical University of Denmark, Denmark*

kye72594@snu.ac.kr, fafnir@snu.ac.kr, tkim@dtu.dk, kjyee@snu.ac.kr

***Abstract*— In order to improve the accuracy of ice prediction code, numerical studies are focusing on the surface roughness which has a significant influence on final ice shape by accelerating turbulence transition and increasing convective heat transfer. Considering the importance of roughness, the fundamental understanding of roughness formation should be investigated. In the present study, an experiment was conducted to observe the early stage of the formation and to obtain quantitative data. Since the initial bead growth occurs microscopically both time and space scale, the experiment was performed under low-speed icing condition where the phenomenon proceeds in macroscale. The close-up images and time-lapse data were obtained, and the typical process of roughness formation was presented through the data. The initial bead growth was emphasized in that it determines the bead size and distribution. As a quantitative analysis, surface coverage, which represents the state of dispersed beads, was characterized by a single parameter. The constant tendency of surface coverage was observed in all test cases and the correlation of surface coverage with the parameter was obtained.**

Keywords— ***Aircraft Icing, Surface Roughness on Ice, Bead Growth, Icing Experiments.***

I. INTRODUCTION

Aircraft icing causes numerous problems such as aerodynamic degradation, structure failure, and safety hazard [1]. In order to avoid a serious accident caused by these problems, the accurate ice prediction is necessary.

In the field of numerical ice simulation, the surface roughness is considered as a crucial factor for improsving the accuracy of icing code [2] – [4]. The attention on surface roughness is due to its significant influence on the icing physics. First, the surface roughness accelerates boundary layer development advancing the turbulence transition of the flow. Since the convective heat transfer is increased in turbulent flow, which is closely related to the energy balance of ice formation, the surface roughness alters the final ice shape substantially. Secondly, surface roughness varies local collection efficiency by changing a droplet trajectory. In particular, as the droplets directly impinge on the initial roughness, the featherlike ice is developed, resulting in the formation of scallop ice on 3D swept wing [5]. Finally, the surface roughness generates local flow perturbation due to its semi-spherical shape. The effect results in the increment of the drag coefficient degrading the aerodynamic performance.

Considering this importance, it is highly required to investigate the fundamental phenomena that contribute the roughness formation. While there are several experimental studies on roughness formation [6] - [10], the understanding of each process is still insufficient. Especially, the early stage of the roughness formation is known to be governed by the bead growth phenomenon [6], [7]. Hence the bead growth process should be investigated in detail.

In the present study, the experimental investigation on bead growth was conducted to broaden the physical insight of roughness formation. Due to the microscale of the early stage of the formation under general inflight icing conditions, the experiment was performed under low-speed icing condition where bead grows in macroscopic scale. Through the experiment, the close-up images and time-lapse data were obtained. In addition, the close-up images were analysed by the image processing method. The quantitative data of initial bead growth were obtained through the method. The data were analysed by the characteristic parameter, which is a well-known parameter in the existing liquid drop growth study [11]. The surface coverage, which is an important indicator of bead distribution, was characterized well by the parameter.

II. METHODOLOGY

A. Experimental Setup

All experiment cases were conducted in Climatic Wind Tunnel (CWT) located in the FORCE Technology, Denmark [12]. The internal view and the blueprint of CWT are shown in Fig. 1. The CWT has a test section of $2\text{m} \times 2\text{m}$ and the maximum velocity of $32\,m/s$. Since the capability of the cooling system depends on the flow velocity, however, the allowable velocity range is narrower than this. For example, at the flow velocity of $25\,m/s$, the lowest temperature is $-5℃$.

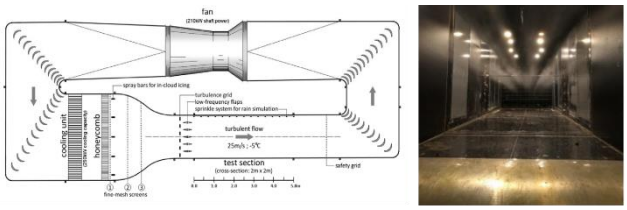

(a) Schematic View of CWT [12] (b) Internal View of Test Section

Fig. 1 Climate Wind Tunnel

The bead growth occurs in the glaze ice condition so that the ambient temperature was set at -7 ℃. The velocity range corresponding to this temperature is below $15\,m/s$. Hence, the test condition was set based on this range and the condition

was validated by CDP-2(Cloud Droplet Probe). The test case is selected as shown in Table 1.

For the test, 2D NACA 0015 airfoil with chord length 0.38m was used. The airfoil was mounted with 4° of AOA. Experiments were conducted for 1, 2, 3, 5, and 20min. It was observed that the spray system has a transition state about 10 seconds in the beginning. Hence, the tests were performed individually. While there are uncertainties in test condition setting, the individual cases were analysed assuming that it shows continuous results. When the ice accretion is completed, the researcher entered the wind tunnel and photographed the beads perpendicular to the airfoil surface over several sections. The temperature was maintained at -7 ℃ during the shooting to prevent melting.

For the experiment with 1, 2, 3, and 5 min close-up bead images were obtained. For 20min case, in addition to the close-up image, 2D ice shape data were obtained. Especially for the case 1, the time-lapse video of 20 min accretion was taken.

Table 1. Test Matrix

Case	Air Speed $[m/s]$	LWC $[g/m^3]$	MVD [μm]
1	10	1.01	19.8
2	10	0.55	25.5
3	10	1.49	21.0
4	10	1	24.3
5	10	1	27.1
6	7	0.714	24.3
7	11.1	0.970	20.8
8	11.1	0.898	23.3
9	11.1	1.347	20.5
10	11.1	0.450	26.8

B. Measurement: Image Processing

Photographs were post-processed by image processing code. In the process, the images were binarized by threshold function detecting the edge of beads. Each bead elements were identified through the process. Irregular bead size was calculated by assuming it as an equivalent circle. Calculated bead diameter was integrated with the bead location. Calibration was done by using the ruler attached on the airfoil.

III. Result and Discussion

In this section, the acquired data and analysis results were presented in the following order. First, the typical process of bead growth observed in the present experiments was described with the close-up picture and time-lapse image. Second, the quantitative analysis of bead growth in the early stage was conducted. The volume weighted average of bead diameter ($\bar{d}_V$) was introduced in order to characterize the spatial variance of bead growth. It was demonstrated that the surface coverage can be characterized only by $\bar{d}_V$ in all cases.

A. Typical Process of Bead Growth

In the present study, since the experiment was conducted under low-speed icing condition, the bead relatively grows on macroscale in time and space. Hence, the detail of the process could be visualized through the photographic data. The most of the images, which are presented here, is data for case 1. Though the only portion of the cases were posted here, these data are the typical representative of other cases.

As shown in Fig. 2, in the early stage of icing, the impinged water remained as a semi-spherical bead. At this moment, the beads covered only part of the surface. Instead, the water that should have covered the surface was concentrated in the bead. It is due to the surface tension acting on the bead. The force balance between flow shear stress and surface tension made the bead stationary.

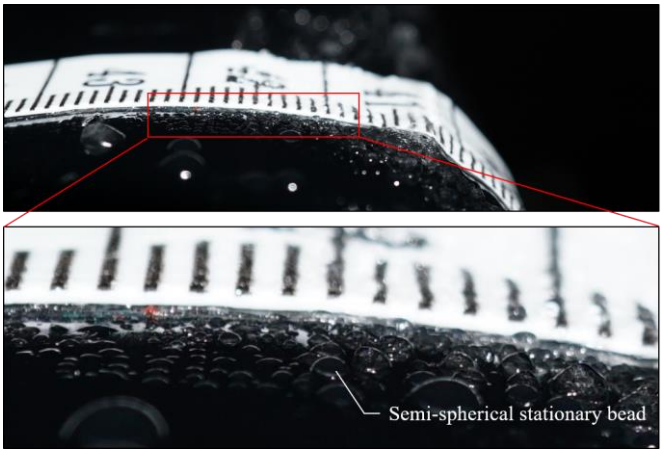

Fig. 2 Close-up Image of Semi-spherical Bead

Since the test condition was glaze condition where the surface temperature close to 0℃, the bead was basically liquid phase and froze partially. As the water impinges, the adjacent beads coalesced each other and were grown into a larger bead. The small beads were created in the space between coalesced beads, which results in a specific distribution pattern that can be observed in Fig. 3.

Fig. 3 Bead distribution for Case1 – 3min at $s/c = 5.47\sim10.73\%$

In addition, it can be observed that the bead distribution is spatially varied along the chord-wise direction in Fig. 3. It is due to the difference in local collection efficiency that decreases toward the trailing edge.

The interesting point from here is that the regions with different time and location have a similar pattern of bead distribution as can be identified in Fig. 4. It means that the region where the droplet impinges at a fast rate with short accretion time (Fig. 4 - (a)) and the region where the droplet impinges at a slow rate with longer accretion time (Fig. 4 – (b)) have similarities in the distribution pattern. It implies that

there is a method to describe the bead distribution in a simple manner.

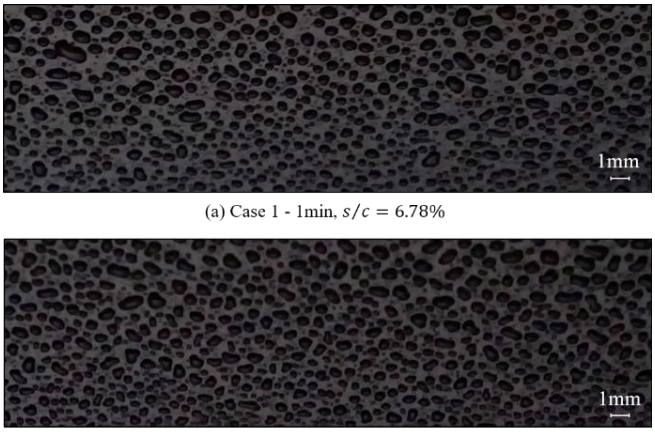

(a) Case 1 - 1min, $s/c = 6.78\%$

(b) Case 1 - 3min, $s/c = 12.05\%$

Fig. 4 Similar Bead Distribution with different case

On the other hands, as the accretion time is over 3min, the size of beads reached a critical size, which is the criteria that the shear force exceeds the surface tension. Then, the bead near the stagnation line began to move first as shown in Fig. 5. The incipient movement caused the bead to coalesce with other beads located on its path and the motion was accelerated. Through this mechanism, rivulet was formed.

Fig. 5 Rivulet Formation on upper surface

As the rivulet swept the bead, the surface water was redistributed. Also, the new bead was created in the swept region. The process is well presented in Fig. 6. It is an image processing data for case 1 - 3, and 5min. The upper boundary corresponds to the location of $s/c = 3.10\%$ and lower boundary corresponds to $s/c = 19.95\%$. The spatial variance of bead can be observed. In particular, the region where rivulet sweeps the bead can be observed in the 5 min case. The re-grown small beads can also be identified in the region.

While the coalescence and the rivulet formation occurred actively in the region away from the stagnation point, however, water film was formed near the stagnation point. It can be observed that there are water films that cover the beads in Fig. 7. In addition, it was identified that the water film broke at the certain point, which is marked as a triangle in Fig. 7. The liquid breakage point was calculated during the image processing. The point was defined as the location where the water film coverage drops to 95%.

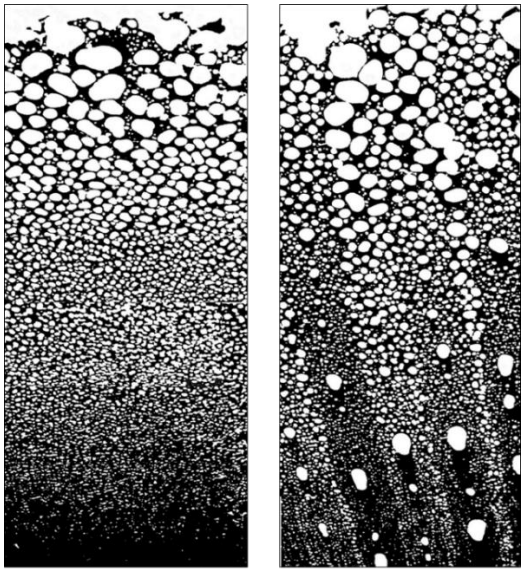

(a) Case 1 – 3min (b) Case 1 – 5min

Fig. 6 Comparison between rivulet case and non-rivulet case on lower surface

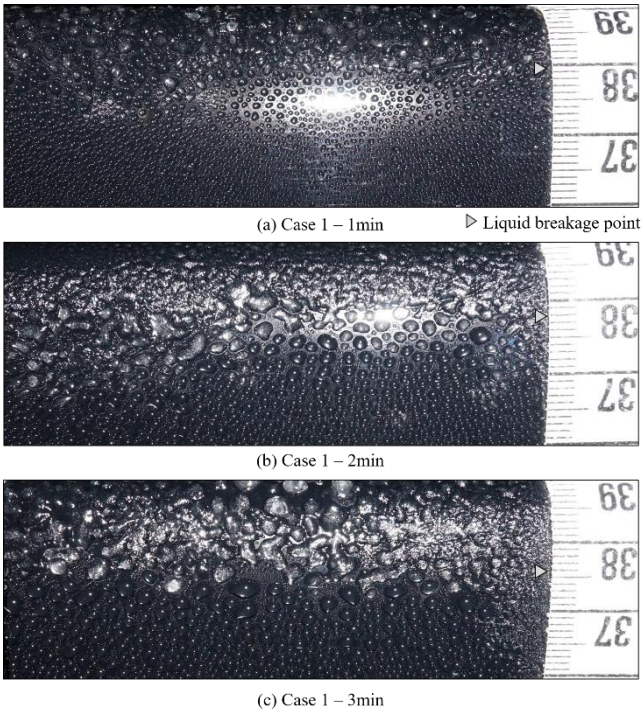

(a) Case 1 – 1min ▷ Liquid breakage point

(b) Case 1 – 2min

(c) Case 1 – 3min

Fig. 7 Water film and Liquid Breakage point in Case 1

In the previous studies, a similar feature is observed as well, which is notated as a stagnation region and collection region [10]. While it is not yet clear how the boundary of the two regions is determined, the tendency that it is proportional to incoming water was confirmed in the present study, as can be expected. In addition, since bead-like roughness was observed

on the film, it is expected that similar physics that governs the bead growth is involved in the stagnation region.

After the initial roughness is formed by beads, rivulet, and water film, the ice and roughness were accreted. Fig. 8 – (a) is the time-lapse data of case 1 for 20 minutes of accretion time. It shows that the stagnation region evolved into a smooth zone whereas the collection region evolved into roughness feather zone, which can be observed in detail in Fig. 8 – (b). In particular, it can be seen that the roughness feather developed in the direction of the flow due to the directly impinging droplet in Fig. 8 – (c). The notable is the fact that the roughness feather was evolved from the bead distribution. It implies the formation of roughness feather is closely related to the initial distribution of beads.

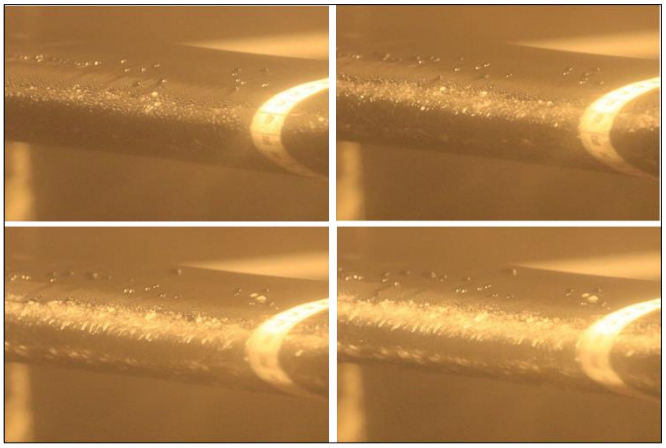

(a) Time-Lapse Images for Case 1 – 20min

(b) Accreted Ice (c) Evolution of Roughness

Fig. 8 The Evolution of Ice and Roughness in Case 1

Up to now, the typical process of bead growth was described through the photographic data obtained from the present study. The initial bead growth, which is predominated by coalescence, is considered important for the following reasons. First, it determines the bead size. It is crucial to check whether it is reached to a critical size. Indeed, the bead size cannot be directly calculated from the amount of water due to its nature that beads cover the surface partially. Therefore, the information of surface coverage is necessary. Second, initial bead growth is involved with the bead distribution. Since the roughness feather is evolved from the distribution, the understanding of initial bead growth is essential in the modelling of the roughness formation.

With this in mind, the quantitative analysis was performed on the initial bead growth. The process was described in the following section.

B. Surface Coverage Analysis

Surface coverage is defined as the ratio between total area and bead covered area. The information of surface coverage is essential because it can be used in the calculation of bead size. However, it is very difficult to present the surface coverage at every position on the airfoil for each icing condition. It is because the bead grows at a different rate and the distribution pattern changes continuously. Hence, it is very important to find a parameter that can characterize the statistical pattern.

In this study, the Volume Weighted Average of Bead Diameter $\bar{d}_V$ was used to characterize the phenomenon. Definition of $\bar{d}_V$ is as follows. d_i is a diameter of a single bead, and V_i is its volume.

$$\bar{d}_V = \frac{\sum V_i d_i}{\sum V_i} \tag{1}$$

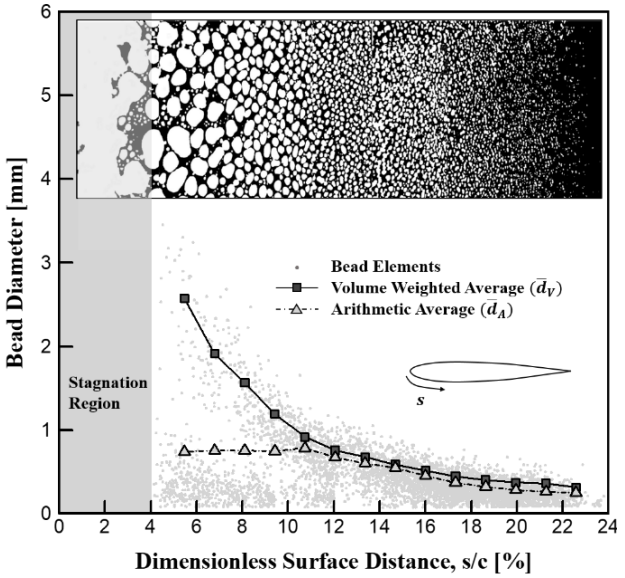

Fig. 9 Comparison between Volume Weighted and Arithmetic Average

Fig. 9 was presented to visually compare the volume weighted average ($\bar{d}_V$) to the arithmetic average ($\bar{d}_A$). Each region was divided into 1cm width and the average was calculated. The image processed data was presented at the top of the graph. The grey points plotted on the graph demonstrates the bead elements. Each axis in x, y order represents the dimensionless chord-wise distance from the leading edge and the bead diameter in a millimeter.

In Fig. 9 the spatial variance of bead is observed. Liquid film region also can be observed near the stagnation point. In the presented case, beads began to be observed from $s/c = 4\%$. The maximum size of bead continuously decreases with the distance from the stagnation point. In particular, it can be observed that the bead distribution is divided into a large bead and small bead ($s/c = 11\%$). The feature is due to the new small beads, merging between the coalesced bead, as described in the previous section.

This characteristic makes the difference in $\bar{d}_V$ and $\bar{d}_A$. At the location farther than $s/c = 11\%$, the $\bar{d}_V$ and $\bar{d}_A$ have a similar tendency. However, at the location closer than $s/c =$

11%, $\bar{d}_V$ follows the overall tendency of large bead whereas $\bar{d}_A$ remains at the value of 0.75mm.

The reason for introducing the parameter is to represent the spatial variance of the bead distribution corresponding to the distance from the stagnation point. In order to meet this goal, the value representing distinct distributions must be different, which is not the case of $\bar{d}_A$. On the other hands, $\bar{d}_V$ satisfies the condition at the region where $\bar{d}_A$ does not. Hence, $\bar{d}_V$ is desirable to be used as a characteristic parameter representing surface coverage.

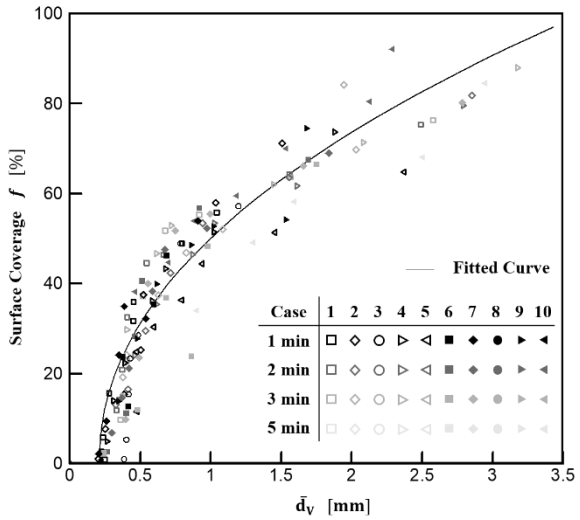

Fig. 10 Surface Coverage with $\bar{d}_V$

The surface coverage of the cases before the occurrence of rivulet was plotted with $\bar{d}_V$ in Fig. 10. The axis in x, y order represents $\bar{d}_V$ and surface coverage f.

In Fig. 10, when $\bar{d}_V$ is smaller than the value of 0.7mm, surface coverage sharply increases with $\bar{d}_V$. On the other hands, when $\bar{d}_V$ is over 0.7mm, the slope of surface coverage gradually decreases. It can be explained by mass conservation during the coalescence. The volume of the bead is proportional to d^3 whereas the surface coverage is proportional to d^2. Hence, the surface coverage is decreased by coalescence given the same amount of water. This description can explain the decrement of the slope.

The interesting point in Fig. 10 is that the surface coverage of the various cases has consistent tendency with $\bar{d}_V$. This means that a universal bead growth property, which is surface coverage here, is characterized by the parameter $\bar{d}_V$ regardless of the test condition of the present experiment.

The surface coverage f was fitted to minimize the error with a fitting function $y = a(\bar{d}_V - b)^c$. The acquired equation is as follows.

$$f = 56.0(\bar{d}_V - 0.21)^{0.47} \quad (2)$$

The equation is shifted by 0.21 because the data cannot capture the beads smaller than a certain limit since they were considered as noise in the image processing. In fact, the surface coverage would be slightly higher than the presented data.

IV. Conclusions

The experimental investigation on roughness formation was performed in the present study. In order to observe the early stage of the formation, which proceeds in microscopic scale both time and space, the experiment was performed in low-speed icing condition where bead grows in macroscopic scale.

Through the acquired close-up photograph and time-lapse data, the detail process of the roughness formation was observed. The spatial variance and the temporal evolution of roughness were captured and the similarity of bead distribution between different region was identified. It was concluded that the initial bead growth is important in that the phenomenon determines the bead size and distribution.

Quantitative analysis was conducted for initial bead growth data. As an analysis method, the volume weighted average of bead diameter ($\bar{d}_V$) was. The surface coverage, which is the important indicator of bead growth, was characterized by $\bar{d}_V$. The constant tendency was observed in all non-rivulet cases.

Further studies should be conducted to quantitatively analyse the initial bead growth properties other than surface coverage. In addition, the correlation between characteristic parameter $\bar{d}_V$ and icing condition is necessary to use the experimental data in other fields of icing such as numerical ice prediction.

Acknowledgment

This work is supported by International joint basic research program from ADD (Agency for Defense Development) of Korea. (UD160053BD)

References

[1] R.W. Gent, N.P. Dart, and J.T. Cansdale, "Aircraft Icing," *Philos. Trans. Royal Soc. A*, vol. 358, pp. 2873-2911, Nov. 2000.

[2] J. Shin, B. Berkowitz, H. Chen, and T. Cebeci, "Prediction of Ice Shapes and Their Effect on Airfoil Performance," *in 29th AIAA Aerosp. Sci. Meet.*, 7-10 Jan. 1991.

[3] G. Fortin, J.I. Laforte, A. Ilinca, "Heat and Mass Transfer during Ice Accretion on Aircraft Wings with an Improved Roughness Model," *Int. J. Therm. Sci.*, vol.45, pp. 595 – 600, 2006.

[4] I.A. Ozcer, G.S. Baruzzi, T. Reid, W.G. Habashi, M. Fossati, G. Croce, "FENSAP-ICE Numerical Prediction of Ice Roughness Evolution, and its Effects on Ice Shapes," *SAE Technical Paper*, no. 2011-38-0024, 2011.

[5] M. Vargas, "Current Experimental Basis for Modeling Ice Accretions on Swept Wings," *J. Aircr.*, vol. 44, no.1, pp. 274-290, May 2007.

[6] W. Olsen, and E. Walker, "Experimental Evidence for Modifying the Current Physical Model for Ice Accretion on Aircraft Surfaces," NASA-TM-97184, 1986.

[7] D.N. Anderson, J. Shin, "Characterization of Ice Roughness from Simulated Icing Encounters," *in 35th AIAA Aerosp. Sci. Meet. Exhibit.*, 6 – 9 Jan. 1997.

[8] R.J. Hansman, S.R. Turnock, "Investigation of Surface Water Behaviour during Glaze Ice Accretion," *J. Aircr.*, vol. 26, no.2, pp 140 – 147, May 1989.

[9] Y. Han, J. Palacios, "Transient Heat Transfer Measurements of Surface Roughness due to Ice Accretion," *in 6th AIAA Atmos. Space Environ. Conf.*, 16 – 20 June 2014.

[10] S.T. McClain, M.M. Vargas, J.C. Tsao, "Characterization of Ice Roughness Variations in Scaled Glaze Icing Conditions," *in 8th AIAA Atmos. Space Environ. Conf.*, 13 – 17 June 2016.

[11] F. Family, and P. Meakin, "Kinetics of Droplet Growth Processes: Simulations, Theory, and Experiments," *Phys. Rev. A*, vol. 40, pp. 3836 – 3854, 1989.

[12] C.T. Georgakis, H.H. Koss, F. Ricciardelli, "Design Specifications for A Novel Climatic Wind Tunnel," *in 8th Int. Symp. Cable Dyn.*, 20 – 21 Sept 2009.